Earth's Future

RESEARCH ARTICLE
10.1029/2022EF002788

Key Points:

- The widespread increase of vegetation greening trend since 1980s was reversed around the year 2000 over 90% of the global vegetated area
- The leveling off of global greenness arisen from recent exceeding optimal temperature and increasing water limitation for photosynthesis
- Our findings of the diversity of browning mechanisms are useful for projecting global future vegetation change and its climatic consequences

Supporting Information:

Supporting Information may be found in the online version of this article.

Correspondence to:

B. Chen and Y. Ke,
baozhang.chen@igsnrr.ac.cn;
yuke@igsnrr.ac.cn

Citation:

Chen, B., Ke, Y., Ciais, P., Zeng, Z., Black, A., Lv, H., et al. (2022). Inhibitive effects of recent exceeding air temperature optima of vegetation productivity and increasing water limitation on photosynthesis reversed global greening. *Earth's Future*, *10*, e2022EF002788. https://doi.org/10.1029/2022EF002788

Received 23 MAR 2022
Accepted 24 OCT 2022

Author Contributions:

Conceptualization: Philippe Ciais, Yiqi Luo
Data curation: Yu Ke, Zhenzhong Zeng, Andy Black, Wenping Yuan, Xiangming Xiao, Junjun Fang, Kun Hou, Ying-Ping Wang, Yiqi Luo
Formal analysis: Yu Ke
Investigation: Yu Ke, Honggang Lv, Mengtian Huang, Junjun Fang
Methodology: Philippe Ciais, Zhenzhong Zeng, Andy Black

Inhibitive Effects of Recent Exceeding Air Temperature Optima of Vegetation Productivity and Increasing Water Limitation on Photosynthesis Reversed Global Greening

Baozhang Chen[1,2,3], Yu Ke[1,4], Philippe Ciais[4], Zhenzhong Zeng[5], Andy Black[6], Honggang Lv[7], Mengtian Huang[8], Wenping Yuan[9], Xiangming Xiao[10], Junjun Fang[1], Kun Hou[1], Ying-Ping Wang[11], and Yiqi Luo[12]

[1]School of Remote Sensing and Geomatics Engineering, Nanjing University of Information Science and Technology, Nanjing, China, [2]State Key Laboratory of Resource and Environmental Information System, Institute of Geographic Sciences and Natural Resources Research, Chinese Academy of Sciences, Beijing, China, [3]University of Chinese Academy of Sciences, Beijing, China, [4]Laboratoire des Sciences du Climat et de l'Environnement, CEA-CNRS-UVSQ, Université Paris-Saclay, Gif-sur-Yvette, France, [5]State Environmental Protection Key Laboratory of Integrated Surface Water–Groundwater Pollution Control, School of Environmental Science and Engineering, Southern University of Science and Technology, Shenzhen, China, [6]Faculty of Land and Food Systems, University of British Columbia, Vancouver, BC, Canada, [7]Key Laboratory of Marine Hazards Forecasting, National Marine Environmental Forecasting Center, Ministry of Natural Resources of the People's Republic of China, Beijing, China, [8]Chinese Academy of Meteorological Sciences, Haidian, China, [9]School of Atmospheric Sciences, Guangdong Province Key Laboratory for Climate Change and Natural Disaster Studies, Zhuhai Key Laboratory of Dynamics Urban Climate and Ecology, Sun Yat-sen University, Zhuhai, China, [10]Department of Microbiology and Plant Biology, Center for Earth Observation and Modeling, University of Oklahoma, Norman, OK, USA, [11]Oceans and Atmosphere, Commonwealth Scientific and Industrial Research Organisation, Aspendale, VIC, Australia, [12]Department of Biological Sciences, Center for Ecosystem Science and Society (Ecoss), Northern Arizona University, Flagstaff, AZ, USA

Abstract Global terrestrial vegetation dynamics have been rapidly altered by climate change. A widespread vegetation greenness over a large part of the planet from the 1980s to early this century has been reported, whereas weakening of CO_2 fertilization effects and increasing climate extremes and the adverse impact of increasing rate of warming and severity of drought on vegetation growth were also reported. Earth system models project that the land carbon sink will decrease in size in response to an increase in warming during this century. How global vegetation is changing during this century in response to global warming and water availability across spatial and temporal scales remains uncertain. Our understanding of the widespread vegetation greening or browning processes and identifying the biogeochemical mechanisms remain incomplete. Here we use multiple long-term satellite leaf area index (LAI) records to investigate vegetation growth trends from 1982 to 2018. We find that the widespread increase of growing-season integrated LAI (greening) since 1980s was reversed (p-value < 0.05) around the year 2000 over 90% of the global vegetated area, and continued in only 10% of the global vegetated area. The reversal of greening trend was largely explained by the inhibitive effects of excessive optimal temperature on photosynthesis in most of the tropics and low latitudes, and by increasing water limitation (increasing in atmospheric vapor pressure deficit and decreasing in soil water availability) in the northern high latitudes (>45°N). Overall, the reversal of greening trend since 2000 weakened the negative feedback of carbon sequestration on the climatic system and should be considered in the strategies for climate warming mitigation and adaptation. Our findings of the diversity of processes that drive browning across bioclimatic-zones and ecosystems and of how those driving processes are changing would enhance our ability to project global future vegetation change and its climatic and abiotic consequences.

Plain Language Summary A widespread vegetation greenness over a large part of the planet from the 1980s to early this century has been reported, whereas weakening of CO_2 fertilization effects and increasing climate extremes and the adverse impact of increasing rate of warming and severity of drought on vegetation growth were also reported. We find that the widespread increase of growing-season integrated LAI (greening) since 1980s was reversed (p-value < 0.05) around year 2000 over 90% of the global vegetated area, and continued in only 10% of the global vegetated area. The reversal of greening trend was largely explained by the negative influence of excessive air temperature on photosynthesis of vegetation growth in most of the tropics and low latitudes, and by increasing in atmospheric vapor pressure deficit and decreasing in soil water availability in the northern high latitudes (>45°N). Our findings of the diversity of browning mechanisms

Resources: Mengtian Huang, Wenping Yuan
Validation: Philippe Ciais, Zhenzhong Zeng
Visualization: Honggang Lv, Mengtian Huang, Wenping Yuan, Xiangming Xiao, Kun Hou, Ying-Ping Wang
Writing – original draft: Yu Ke, Yiqi Luo
Writing – review & editing: Philippe Ciais, Zhenzhong Zeng, Andy Black, Wenping Yuan, Xiangming Xiao, Ying-Ping Wang, Yiqi Luo

across bioclimatic-zones and ecosystems are useful for projecting global future vegetation change and its climatic and abiotic consequences.

1. Introduction

Terrestrial vegetation plays a key role in the exchange of carbon, water, momentum and energy between the land and the atmosphere (Baldocchi et al., 2001; Bonan et al., 1992; Haberl et al., 2007; Law et al., 2002; Piao et al., 2020; Zhu et al., 2016), and has accounted for more than half of the global carbon sink since the 1960s, which substantially mitigated climate warming (Forzieri et al., 2017; Jung et al., 2017; Wang et al., 2020). Long-term temporal changes in leaf area index (LAI; leaf area per unit ground area), as a key indicator of vegetation growth that largely controls land-climate interactions and feedbacks (Forzieri et al., 2017), has elicited considerable interest from scientists and policymakers (Piao et al., 2020). Long-term changes in vegetation are driven by multiple interacting drivers including the atmospheric CO_2 fertilization effects, nitrogen deposition and regional climate change (temperature, precipitation, radiation, and humidity) (Cox et al., 2000; Forzieri et al., 2017; Piao et al., 2020; Zhu et al., 2016). A persistent and widespread increase of growing season integrated LAI over 25%–50% of the global vegetated area during the period 1982–2009 has been reported (Zhu et al., 2016), whereas other studies have reported a stalling or even a reversal of the greening trend since 2000 (Chen et al., 2014; de Jong et al., 2012; Feng et al., 2021; Piao et al., 2011; Tian et al., 2015). Tropical temperatures are reported to be close to the optimal photosynthetic temperature of trees (Corlett, 2011; Huang et al., 2019), and consequently rising tropical temperatures could limit vegetation growth. Meanwhile, warming has been found to facilitate increasing vegetation growth over the high latitudes instead of being a climatic constraint on growth (Lucht et al., 2002; Xu et al., 2013). In the northern hemisphere the response of vegetation growth to temperature exposure enhanced convergently with increasing temperature before plant functional type-dependent temperature thresholds were reached (Feng et al., 2021). CO_2 fertilization was thought to be a major factor driving vegetation greening at the global scale (Piao et al., 2020; Zhu et al., 2016), while CO_2 fertilization effects on vegetation photosynthesis has recently been reported to have declined across most terrestrial regions of the globe since 2001 (Wang et al., 2020). More recently atmospheric vapor pressure deficit (VPD) was reported to have worldwide impacts on the interannual variability of terrestrial carbon uptake (Corlett, 2011). A full understanding of the long-term vegetation growth changes and their drivers over the last four decades across spatial scales and biomes is therefore still lacking (Jung et al., 2017; Piao et al., 2020).

Here, we investigate trends of LAI and their drivers for the longest, continuous data series of 1982–2018 based on an assemble of remotely sensed data sets (AVHRR, GIMMS LAI3g, and GLASS) using a commonly used best-fit trend breaks approach including three statistical analysis models (Chen et al., 2014) (a simple linear regression model, a breakpoint [BP] model and a turn-point [TP] model, see Section 2) to identify a reversal point (RP). We first analyze vegetation growing trends at both global and pixel scales using growing season integrated LAI. We use three statistical analysis models to detect the mechanism of vegetation dynamics from 1982 to 2018 and then apply the Akaike information criterion (AIC) method to choose the best fit model at each pixel across the globe (Chen et al., 2014). Only pixels with no or slight land-cover changes during the study period were included in our analyses (Figure S1 in Supporting Information S1).

2. Data and Methods

2.1. Leaf Area Index Data

The latest gridded daily LAI data used in this study were obtain from the NOAA Climate Data Record (CDR) of AVHRR LAI and Fraction of Absorbed Photosynthetically Active Radiation (FAPAR), Version 5 (https://data.noaa.gov/dataset/dataset/noaa-climate-data-record-cdr-of-avhrr-leaf-area-index-lai-and-fraction-of-absorbed-photosynthet), which was derived and maintained by the CDR program of NOAA Advanced Very High-Resolution Radiometer (AVHRR) Surface Reflectance onboard the NOAA 7, 9, 11, 14, 16, and 18 platforms. These global LAI data were used to detect interannual variations of vegetation growth during 1982–2018. The Artificial Neuron Network (ANN) model was trained with nadir-adjusted surface reflectance to retrieve LAI, then using the BEnchmark Land Multisite ANalysis and Intercomparison of Products (BELMANIP-2) and DIRECT network sites to validate the quality of this product. The AVHRR LAI product has a spatial resolution of 0.05° and a daily temporal resolution spanned from 1981 to present. According to the attached QC data, we

first excluded snow, water, cloud cover and other invalid pixels from our analysis and averaged daily LAI to monthly intervals. Then, neighboring pixels in spatial-temporal scales could linearly interpolate gaps to ensure enough gridded values in each year. Pixels with averaged LAI values during 1982–2018 less than 0.1 are treated as non-vegetated land and would not be included in further calculation following Fang et al. (2019). To reduce the uncertainties that may stem from one remote sensing data set, the other LAI products, the Global Land Surface Satellite (GLASS) and the Global Inventory Modeling and Mapping Studies (GIMMS), were also analyzed simultaneously. The GLASS LAI data set, with spatial resolutions of 0.05° and temporal resolutions of 8 days (http://www.glass.umd.edu/Download.html) was produced using MODIS and AVHRR land surface reflectance via Generalized Regression Neural Network (GRNNs) model, and the accuracy was evaluated by comparing with other LAI products such as MODIS and CYCLOPES, as well as field measurements. The GIMMS LAI data set, named LAI3g, was generated based on AVHRR GIMMS NDVI3g, MODIS LAI datasets using a Feed Forward Neural Network (FFNN) model with a composited temporal resolution of 15 days and a bi-cubic resampled spatial resolution of 1/12° (http://sites.bu.edu/cliveg/datacodes/). Evaluation of this product also utilized LAI products for other satellites and field measurements. Using the same way of processing AVHRR LAI, the two products can be composited to multi-year global LAI means (1982–2018 of GLASS, 1982–2016 of LAI3g). Due to the uncertainties in different LAI products, especially interannual trend fitting, the averaged value of the three products at a pixel level was calculated for overall analysis. The means for 2017 and 2018 were only produced by AVHRR and GLASS datasets because of the insufficient time series in LAI3g.

2.2. Climate and Soil Moisture Data Set

In order to explore drivers of global LAI trend changes, the global gridded daily maximum air temperature (T_{air}^{max}), VPD and root zone soil wetness (RSW) were selected in this study. Specifically, T_{air}^{max}, daily mean air temperature (T_{air}^{mean}) and actual vapor pressure (VAP) at a spatial resolution of 0.5° from 1982 to 2018, were obtained from the Climatic Research Unit (CRU) Time-Series (TS) version 4.03 of high-resolution gridded data of month-by-month variation in climate (https://crudata.uea.ac.uk/cru/data/hrg/). The last two variables were utilized to calculate monthly VPD.

2.2.1. Air Temperature Data

The T_{air}^{max} is calculated arithmetically by the gridded absolute values of T_{air}^{mean} and diurnal 2-m temperature range (DTR) with the formula as T_{air}^{mean} + 0.5* DTR, then averaging daily maximum air temperature rather than extracting the maximum temperature in each month. For discussing the dominant influence of growing-season $T_{air}^{max,gs}$ on interannual trends of LAI referenced by ref (Huang et al., 2019), the monthly T_{air}^{max} data set in each year, through temporally linear interpolation, were filled into 8-day intervals in the determined averaged 37-year growing season range at pixel scales to obtain ecosystem optimum temperature by combining with LAI data at 8-day intervals (Zhu et al., 2016).

Vapor Pressure Deficit Data Set

The monthly VPD data set was calculated using saturated vapor pressure (SVP) and VAP through the following model (Yuan et al., 2019):

$$\mathrm{VPD} = \mathrm{SVP} - \mathrm{VAP} \tag{1}$$

$$\mathrm{SVP} = 6.112 \times \left(1.0007 + 3.46 \times 10^{-6} P_{\mathrm{mst}}\right) e^{\frac{17.67 T_{\mathrm{mean}}}{T_{\mathrm{mean}} + 243.5}} \tag{2}$$

$$P_{\mathrm{mst}} = P_{\mathrm{msl}} \left(\frac{T_{\mathrm{mean}} + 273.16}{T_{\mathrm{mean}} + 273.16 + 0.0065 \times Z} \right)^{5.625} \tag{3}$$

where Z represents the altitude of each grid-point (m) (https://cds.climate.copernicus.eu/). P_{msl} and P_{mst} are the standard air pressure (set as 1013.25 hPa) and air pressure, respectively. The VAP product is generated from station anomalies of T_{air}^{mean} and DTR. All variables were obtained from CRU website.

2.2.2. Root Zone Soil Wetness Data Set

The monthly RSW data were obtained from Modern-Era Retrospective analysis for Research and Applications Version 2 (MERRA-2) with a spatial resolution of 0.5° × 0.625° from 1982 to 2018 (https://climatedataguide.

ucar.edu/variables/land/soil-moisture) (Gelaro et al., 2017). Compared with surface soil moisture, the RSW is more closely related to water availability to plants. This data set represents the soil water content proportion below the land surface at a depth of 0.1–1.0 m, and was aggregated to a spatial resolution of 0.5° using a nearest neighbor method. Same as for T_{air}^{max}, VPD and RSW were restricted to the growing season range, as well as interpolating to 8-day intervals by a linear method pixel by pixel.

2.3. Extraction of Unchanged Plant Areas

The GLASS-GLC product is used in this study to mask unchanged land cover (LC) to minimize the impact of LC change on LAI changing trends (https://doi.pangaea.de/10.1594/PANGAEA.913496). This product was generated by GLASS CDRs using the random forest classifier on the Google Earth Engine (GEE) platform with a spatial resolution of 5-km (Liang et al., 2013; Liu et al., 2020). The overall accuracy with global forest, cropland, grassland, shrubland, tundra, barren land and snow/ice is about 82.81%. Based on this data set, we selected pixels as unchanged land when the frequency of land cover change is lower than 3 years from 1982 to 2018 after eliminating snow/ice and water pixels. Due to the GLASS-GLC product lacking detailed sub-classification of forest, the synGLC product (Xu et al., 2014) with a spatial resolution of 8-km (https://synglc.xuguang.info/#Intro), integrated information from five land cover products such as MCD12Q1 and GLC2000, was employed to fit the five forest types, including evergreen broad-leaf forest (EBF), deciduous broadleaved forest (DBF), evergreen needle leaved forest (ENF), deciduous needle leaved forest (DNF) and mixed forest (MF), into corresponding unchanged pixels of the GLASS-GLC product. We then produced the unchanged plant area data set with nine classes. If pixels did not match forest types for the two products, we chose GLASS-GLC classes data. Only pixels classified as forest in GLASS-GLC and any types of forest in synGLC can be transformed and replaced.

2.4. Extraction of Growing Season Phenology

The study focuses on the LAI in growing season and it was extracted following researches (Zhu et al., 2016). Considering the missing daily values of AVHRR LAI products, to reduce the uncertainty of plant growing season extraction, we first interpolated the 8-day GLASS LAI data linearly to daily intervals, then the Savitzky-Golay filter was utilized to do data smoothing. From the beginning of each year, the start date of growing season was determined when the value of LAI reaches the 15% of overall amplitude and exceeds 0.1 m^2 m^{-2}. The end time of growing season was determined when LAI fulfills the conditions of 15% of overall amplitude and exceeds 0.1 m^2 m^{-2}, with this time should be after the date corresponding to the maximum (see Figure S18 in Supporting Information S1 as an example). Eventually, the growing season length for every year can be defined as the span between the start and end dates, while the 37-year average was regarded as overall growing season length. Because of the lag of the growing season in the southern hemisphere, the yearly calculation was based on 2-year LAI datasets and the range was restricted in 365 days, particularly the start and end dates for EBF were simply set as 1 and 365, respectively. Finally, the start and end dates of growing season during 1982–2018 were derived from the global gridded LAI data set (Figure S19 in Supporting Information S1).

2.5. LAI Trend Detection

To better detect whether the plant growing trend has changed, three statistical analysis models (Chen et al., 2014), including a simple linear regression model, a BP model and a turning-point model, were used in this study to depict changing characteristics of vegetation growth from 1982 to 2018 following ref. Chen et al. (2014). The AIC (Akaike, 1974) was used to measure the goodness of the three statistical fitting models. Decided by residual sum of squares, number of data and parameters of the model, a smaller AIC means a better fitting, and the detailed description of the use of AIC can be found in ref. Chen et al. (2014).

The fitting parameters obtained from the three models, after selecting using significance and R^2, could calculate the respective AIC values. The AIC value is used to determine which of these three models preferentially fit the time series of LAI data whether either the BP or TP is significant.

2.6. Estimation of Ecosystem Optimum Temperature for Photosynthesis (T_{opt}^{eco})

Air temperature, by affecting the enzyme activity and leaf surface stoma, directly controls plant photosynthesis. It has been reported that photosynthetic capacity increases with temperature up to an optimum temperature with a typical range of 30°C–40°C, and the optimum temperature for leaf-scale photosynthesis (T_{opt}^{leaf}) varies with plant species, climates, soil nutrients (Kattge & Knorr, 2007). The optimum air temperature for ecosystem-level gross primary productivity (T_{opt}^{eco}) differs from T_{opt}^{leaf} and is important for improving the representation of ecosystem-scale photosynthesis (Field et al., 1995; Huang et al., 2019; Liu, 2020). To analyze the relationship between air temperature and global long-term changes in LAI, we first estimated local T_{opt}^{eco} by examining the temperature response curve of AVHRR LAI. We chose the higher LAI with the corresponding T_{air}^{max} in a narrow growing season instead of the whole length of the growing season range to analyze if the air temperature with the best plant growth exceeds the optimum temperature, also minimizing the uncertainties generated by the extraction process through eliminating the values of the first and the last months regarded as extracted boundaries. The values of LAI out of the shortened growing season and $T_{air}^{max} <$ °C were deleted based on plant physiology. Following Huang et al. (2019), growing season LAI time series throughout the entire monitoring period and the corresponding temperature data were grouped into 0.5°C temperature bins for each vegetated pixel. In each pixel, we created different T_{air}^{max} bins and put relevant LAI values into them according to the step size of 0.5°C confined by maximum and minimum, with gradually increasing of T_{air}^{max}. The 85th percentile LAI was chosen as representative in each temperature bin to minimize the uncertainty of the impact of environmental factors. We then calculated the running means of every three temperature bins to develop the temperature response curve of LAI. Eventually, the T_{opt}^{eco} was determined from the response curve at which LAI was maximized for a specific vegetation pixel (Figure S20 in Supporting Information S1). Note that T_{opt}^{eco} may not be detected for some pixels where the maximum LAI was only attained at either end of the response curve, accounting for 2.3% of the vegetated areas. The failed pixel number using 85th percentile as a threshold is lower than using 90th percentile by Huang et al. (2019) (2.3% vs. 3.5% of the vegetated areas globally). Following Huang et al. (2019), we also applied nonlinear regression analysis of daily LAI against daily maximum air temperature (T_{air}^{max}) to estimate T_{opt}^{eco} for each PFTs pixel by pixel, which produced similar results.

2.7. The Main Environmental Factors Controlling LAI Trend Changes

To interpretate the existence RPs of LAI at high latitudes where plant growth has not been suppressed by temperature, we estimated the contributions of the environmental factors, $T_{air}^{max,gs}$, VPD and root-zone soil wetness (RSW), to LAI trend changes using a multiple linear regression modeling approach (Figure 4, Figures S12–S16 in Supporting Information S1). This approach was used to partition the contributions of T_{air}^{max}, VPD and RSW to LAI trend changes during 1982–2018 as in the following equations (He et al., 2019):

$$\mathrm{LAI} = a_1 T_{air}^{max,gs} + a_2 \mathrm{VPD} + a_3 \mathrm{RSW} + \varepsilon \tag{4}$$

$$k_x = \frac{d\,(a_i \times x)}{dt} \quad x \in \left\{T_{air}^{max,gs},\ \mathrm{VPD},\ \mathrm{RSW}\right\};\ i \in \{1,2,3\} \tag{5}$$

where a_1, a_2, and a_3 represent the sensitivity of LAI change to $T_{air}^{max,gs}$, VPD and RSW. The product, $a_i \times x$, can be considered to be the contribution of variable x to LAI, so k_x in Equation 5, expressed as the change of this product with time, represents the contribution of variable x to LAI trend change. Air temperature, atmospheric VPD and soil water availability usually co-vary in time and space, so partial regression coefficient in multiple linear regression model (Equation 4) could be mis-interpreted. We calculated the variance inflation factor (VIF),

$$\mathrm{VIF}_i = 1 - \left(1 - R_i^2\right) \tag{6}$$

where i is one of these three variables ($T_{air}^{max,gs}$, VPD, and RSW), and VIF_i and R_i are VIF and correlation coefficient of i against other two variables. As shown in Figure S21 in Supporting Information S1, we observed the pixels with the VIF values of the three variables less than the threshold of 5 over the global for the period before and after the RPs account for 81% and 71%, respectively. Generally, five is used as the threshold: if VIF <5 indicates that there is no collinearity problem (Akinwande et al., 2015). Our analysis suggests multicollinearity of three factors is relatively low.

3. Results

3.1. Recent Global Break-Off and Decline of Greenness

Widespread break-off and decline of vegetation greenness were consistently revealed by a trend breaks analysis approach from the three long-term satellite LAI data sets (Figures 1a–1d). The ensemble mean of the three data sets shows that for more than 91.60% of global vegetated area there exists a RP (either BP: 56.5 ± 1.45%, or TP: 34.1 ± 2.09%) during the past four decades (Figure 1e), which mainly occurred during 1998–2005 with an ensemble mean occurrence year of BP of 2001 and TP of 2000 (Figures S2b, S3b, and S4b in Supporting Information S1). The LAI3g LAI data show the most extensive statistically significant existing RP data (Mann–Kendall test, $p < 0.01$ [0.05]) covering over 65.5% (51.0%) of vegetated lands, followed by AVHRR LAI (58.7% [45.0%]) and GLASS LAI (53.6% [40.3%]) (Figure 1e). All three LAI data sets also consistently show a gradually increasing LAI trend (best fit linear model, greening) over less than 9.4% of global vegetated land (Figure 1e). Overall, the BP model detected RPs predominantly across the globe, while the TP model detected RPs mainly in the northern Eurasia, central Africa and southern north America (Figures S2–S4 in Supporting Information S1). The global ensemble median trends in the growing season LAI before BP and TP were 0.0942 (95% CI (confident interval): 0.0936–0.0947) and 0.1007 (95% CI: 0.1000–0.10134) $m^2\ m^{-2}$ $decadel^{-1}$, while after the RPs of the BP and TP models were −0.0053 (95% CI: −0.0044 to −0.0061) and −0.0559 (95% CI: −0.0576 to −0.0542) $m^2\ m^{-2}$ $decadel^{-1}$, respectively (*t*-test, trends before and after BP are significant different, $p < 0.1$, Figures 1f and 1g, Figures 2a and 2b, Figures S5a and S5b, and Figures S6a and S6b In Supporting Information S1).

We next calculated the time series of trends in the growing season LAI with 15-year moving windows during 1982–2018 (Figure 1h). We found that the global mean trends significantly increased from 1982 to 2003 and then decreased to 2011 and then stalled to date based on the AVHRR and GLASS data sets; and the GIMMS LAI3g shows that the trends kept on decreasing from 1982 to 2010 at a rate of −0.016 $m^2\ m^{-2}$ $decadel^{-2}$, and then stalling to 2018.

As shown in Figure 2 and a Figures S5–S6 in Supporting Information S1, the three data sets consistently show positive and negative values over a large proportion of the global vegetated land during the periods before and after the RPs, respectively. Before the RPs, the pronounced growth spread over most of six continents, especially over the mid-low latitudes such as south Asia and north Africa primarily controlled by the BP model. Whereas vegetation browning (i.e., LAI decreasing) remarkably occupied western North America and Amazon regions. It was reported that the inferior data quality caused by cloudy over Amazon may cause a great deal of trend uncertainty and affect the fitting results between different LAI products (Chen et al., 2019; Forzieri et al., 2017). The global ensemble median trends in the growing season LAI before the RPs estimated from the three data sets are 5.91 ± 3.34% $decadel^{-1}$ (0.090 ± 0.241 $m^2\ m^{-2}$ $decadel^{-1}$), with 6.16 ± 3.85% (0.094 ± 0.235) and 6.58 ± 4.18% (0.100 ± 0.275) of BP and TP, respectively. After the RPs, however, LAI decreased over most of vegetation land in the world with global ensemble mean trends values estimated from the three data sets of 0.051 ± 0.915% $decadel^{-1}$ (0.008 ± 0.371 $m^2\ m^{-2}$ $decadel^{-1}$), with 0.344 ± 0.357% $decadel^{-1}$ (0.005 ± 0.042 $m^2\ m^{-2}$ $decadel^{-1}$) and −3.655 ± 0.484% $decadel^{-1}$ (−0.056 ± 0.025 $m^2\ m^{-2}$ $decadel^{-1}$) of BP and TP, respectively. The LAI changing speed appeared to slow down slightly compared to the first segment (before RPs). Whereas, vegetation greening occurred in China, west of Europe, southeast of North and part of south America (Figure 2 and Figures S5 and S6 in Supporting Information S1). A strikingly greening pattern prominent in China and India was attributed mainly to national programs to conserve and expand forests of China and multiple cropping facilitated by fertilizer use for both of China and India (Chen et al., 2019). The exceptional greenness was mainly driven by Human land use and browning was dominated by climate change.

Comparatively, the trends kept relatively stable after the RPs obtained using the TP model with all slopes less than or near 0, and the trends after the RPs obtained using the BP model dramatically varied across different latitudes, indicating conspicuous regional heterogeneity of vegetation growth dynamics. There were abrupt transitions over the lower latitudes, in the northern hemisphere and the equatorial regions.

The three data sets also consistently show that the global averaged vegetation trends before RPs for all plant functional types (PFTs) were significantly higher than those after RPs and most of PFTs showed negative median values of linear trends after RPs (Figure 2c, Figures S5c and S6c; Tables S1 and S2 in Supporting Informa-

10.1029/2022EF002788

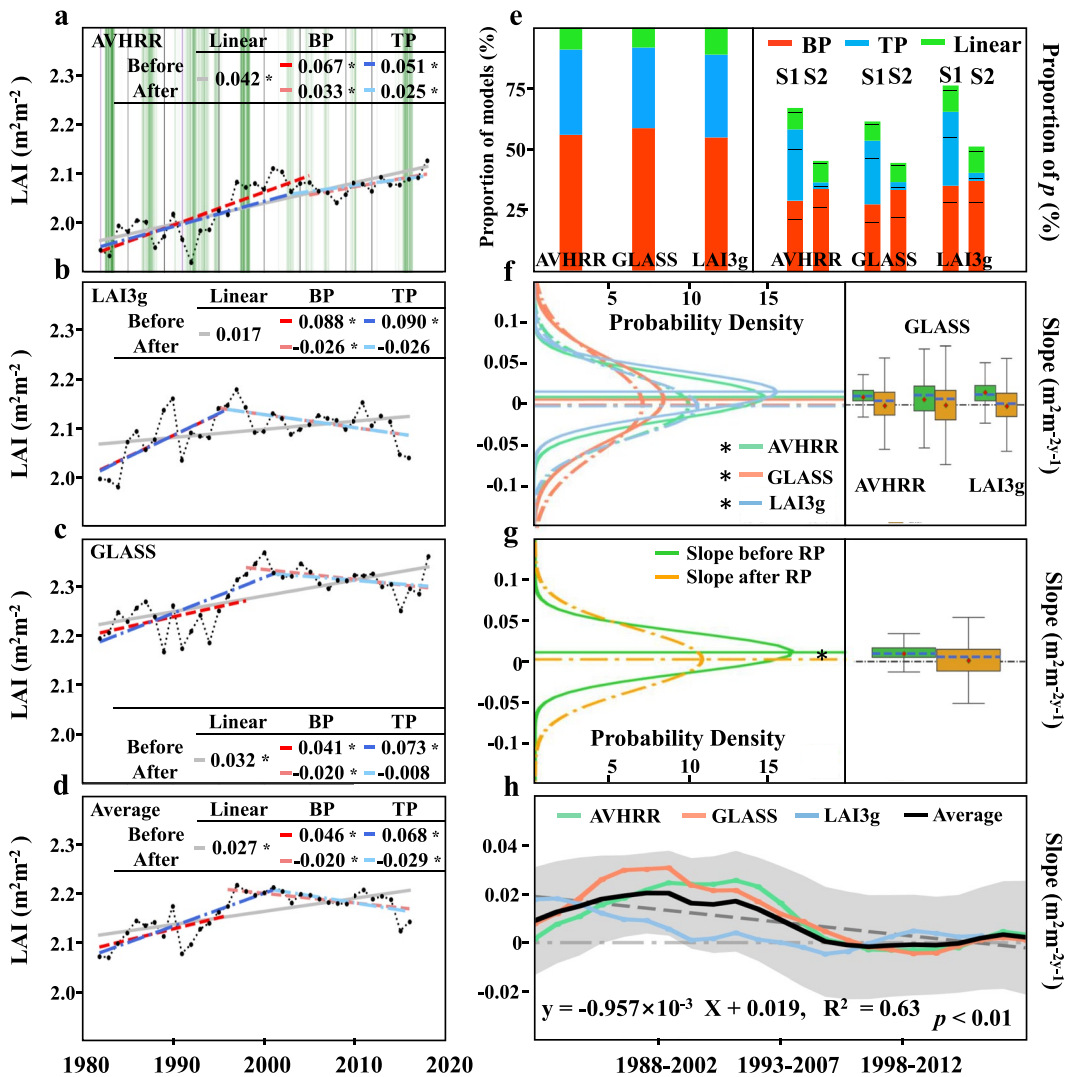

Figure 1. Break-off and decline of global greenness from around 2001. (a–d) Interannual changes and trends in global mean growing season integrated leaf area index (LAI) of the three remote sensing data sets (a, AVHRR, b, GIMMS3g, c, GLASS, and d, the ensemble averages of these three data sets) for the period 1982–2018. In a, the green shaded area shows the intensity of the EI Niño–Southern Oscillation (ENSO) as defined by the multivariate ENSO index. The gray lines label the sensor changing time of the AVHRR satellite series. Two volcanic eruptions (El Chichón eruption and Pinatubo eruption) are indicated by pink lines. (e) The histograms show the percentage of pixels with the best fitting model among the three models (linear, breakpoint and turn-point models) over the global vegetation pixels (left) and pixels only with statistically significant levels at $p < 0.1$ (right); the horizontal black lines in each of the columns on the right indicate significant levels at $p < 0.05$. A standard Akaike information criterion (AIC) was used to choose the optimal fitting model (see Section 2). S1 and S2 indicate the statistical results for the periods before and after the reversal points (RPs), respectively. (f) (left) Probability density function of growing season LAI trends (slopes) before (solid line) and after (dashed line) the RPs derived from the three LAI data sets. (right) Boxes represent the interquartile ranges of the trend values (solid lines represent medians), and whiskers extend to one time the interquartile range. Median trend values for the two periods before (green) and after (yellow) the RPs and their s.d. are shown in Tables S1 and S2 in Supporting Information S1. The asterisk indicates a significantly different trend between the two periods, on the basis of a two-sample Kolmogorov-Smirnov test at $p < 0.01$. (g) Same as (f) but for the ensemble average of these three data sets. (h) Temporal dynamics of trends for the three LAI data sets with 15-year moving windows during 1982–2018. The gray area indicates 1 SD on either side on the mean (n = 485,673).

tion S1). We further simply compared the 5-year interval's averages of growing season LAI at pixel levels with the reference period's value of LAI for 1998–2005 when RPs mainly occurred. The three data sets also consistently show that LAI increased before RPs while decreased after RPs for most of the global vegetated area (Figures S7–S9 in Supporting Information S1).

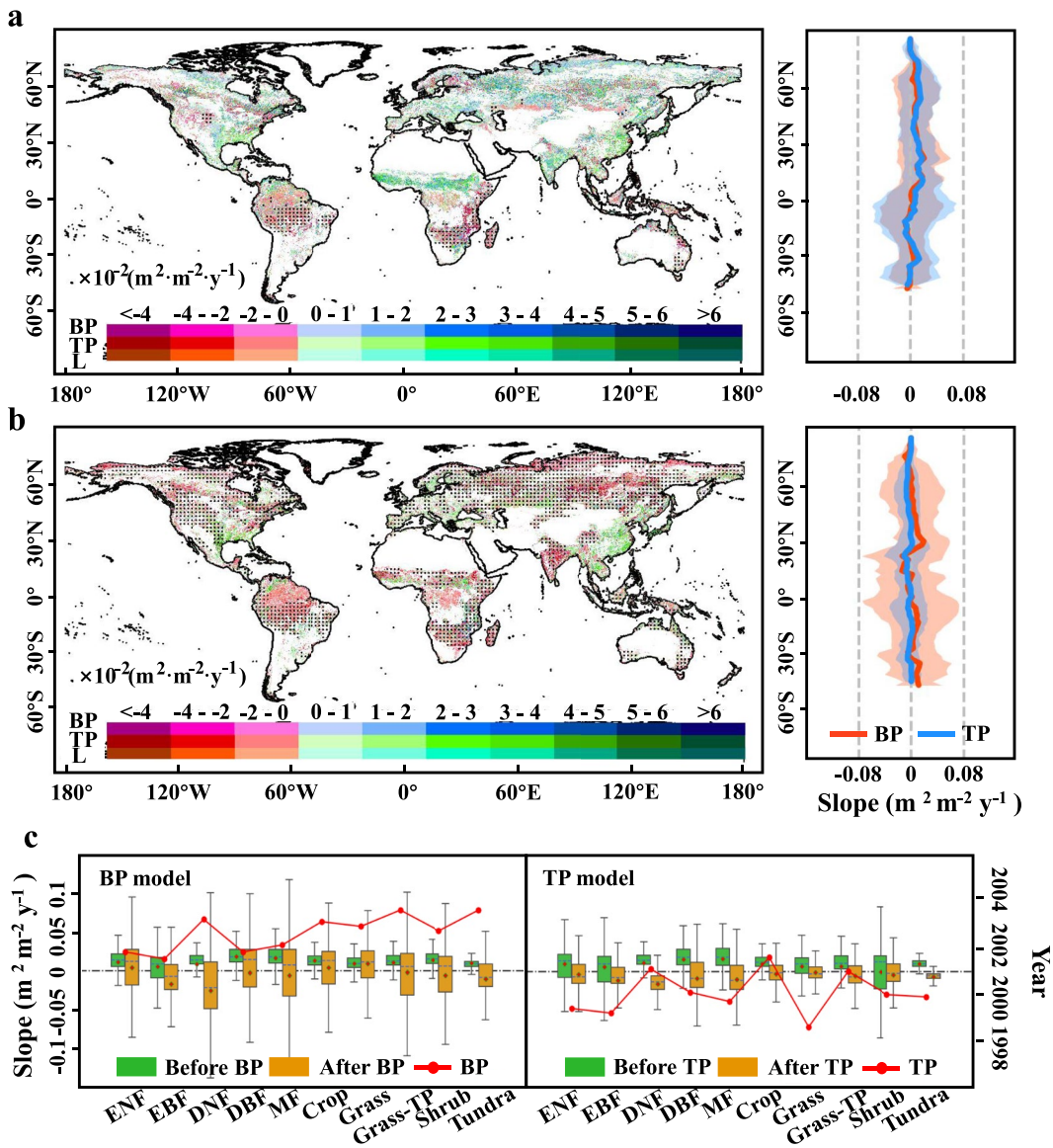

Figure 2. Trends in observed growing season integrated leaf area index (LAI) before (a) and after (b) the reversal points derived from the AVHRR LAI data set. The right panels in (a) and (b) show the latitude's averages of trends calculated by the breakpoint (BP) and turn-point (TP) models. The Mann-Kendall test was used to estimate the trends at pixel levels, and the regions with black dots indicate significant trends ($p < 0.1$) with pixel size of 0.05°. (c), Boxes represent the interquartile ranges of the global averaged vegetation trends for particular plant functional types (solid lines represent medians), and whiskers extend to one times the interquartile range. The left and the right panels are for the BP and TP models, respectively. The green and yellow boxes are the trends (slopes) before and after reversal points, respectively. ENF: Evergreen needle-leaf forest; EBF: evergreen broad-leaf forest; DNF: deciduous needle leaf forest; DBF: deciduous broad-leaved forest; MF: mixed forest; Grass-TP: grass land in Tibetan Plateau.

4. Discussion

Photosynthetic capacity increases with temperature up to an optimum temperature (T_{opt}) at both leaf (Kattge & Knorr, 2007; Lloyd & Farquhar, 2008) and ecosystem (Huang et al., 2019; Liu, 2020) scales. Above T_{opt}, photosynthetic capacity sharply declines as electron-transport and Rubisco enzymatic capacities become impaired (Huang et al., 2019), stomatal closure in leaves increases (Williams et al., 2013) and partial hydraulic failure occurs owing to warming-induced water stress (Tyree & Dixon, 1986). The ecosystem-level optimum temperature of photosynthesis (T_{opt}^{eco}) is latitude- and PFTs-dependent, with higher values at lower latitudes than in colder

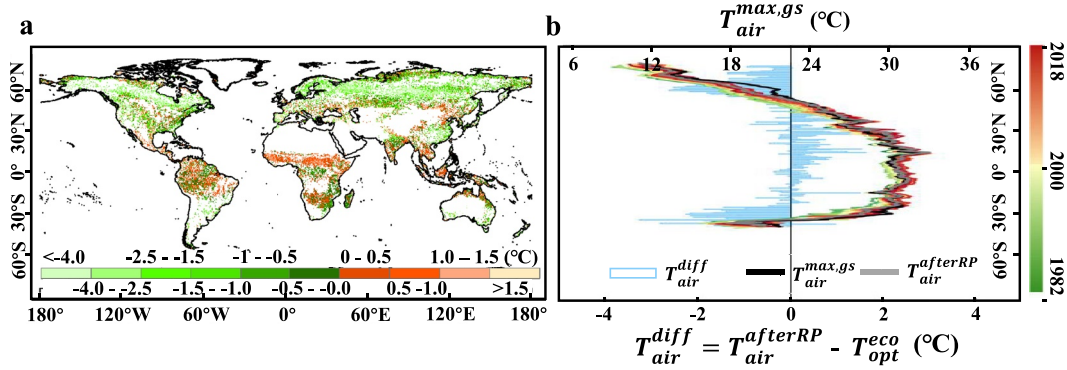

Figure 3. Comparison of growing season mean daily maximum air temperature ($T_{air}^{max,gs}$) and ecosystem optimum temperature for photosynthesis (T_{opt}^{eco}). (a) Global spatial distribution of the difference between multi-year average of $T_{air}^{max,gs}$ for the years after occurrence of reversal points (RPs) and T_{opt}^{eco}. b, Latitudinal averages of annual $T_{air}^{max,gs}$ from 1982 to 2018 (gradient ramp), of multi-year average of $T_{air}^{max,gs}$ after RPs ($T_{air}^{afterRP}$, gray line), of T_{opt}^{eco} (black line). The latitudinal differences (T_{air}^{diff}) between the multi-year average of $T_{air}^{max,gs}$ for the years after RPs ($T_{air}^{afterRP}$) and T_{opt}^{eco} are shown in blue hollow bars, where $T_{air}^{diff} = T_{air}^{afterRP} - T_{opt}^{eco}$. The global distributions of T_{opt}^{eco} and $T_{air}^{afterRP}$ are shown in Figure S10 in Supporting Information S1.

regions, and air temperature of the growing season has recently been approaching to T_{opt}^{eco} (Huang et al., 2019). Experimental evidence of the saturation of CO_2 fertilization effect on vegetation photosynthesis, together with a global decline of CO_2 fertilization effects on vegetation photosynthesis from this century (Wang et al., 2020), suggest a limited buffering capacity of the Earth greening under climatic warming (Feng et al., 2021; Huang et al., 2019). Viewed at the global scale (Figure 3, Figure S10 in Supporting Information S1), our study demonstrates the daily maximum air temperature in growing season (T_{air}^{max}) sustained the increase from global average of 23.06°C in 1982 to 24.09°C in 2018, which has not yet exceeded global average T_{opt}^{eco} of 24.67°C, but in warmer regions ($T_{air}^{max,gs} > 25$°C), $T_{air}^{max,gs}$ has been very approaching to or higher than T_{opt}^{eco} since the start of this century (Figure S10 in Supporting Information S1). We found that the pixels with $T_{air}^{max,gs}$ exceeding T_{opt}^{eco} are mostly located at lower latitudes (45°N ~ 30°S), such as central Africa, south North America, north South America, and south Asia, accounting for 41.1% of the global vegetated area (=26.9 million km^2), where the air temperature restricted LAI growth after the RPs (Figure 3, Figure S10, Tables S1 and S2 in Supporting Information S1).

The restriction of vegetation growth due to increasing growing season air temperature is PFTs dependent as well. As shown in Figure S11 and Table S3 in Supporting Information S1, the reversals of vegetation greening by air temperature restriction were found in evergreen EBF in NH1 (20°S–0°S) and NH2 (20°N–50°N), crop land in NH1 and NH2, grass land in NH1 and SH1 (20°S–0°S), Shrub land in SH1 and SH2 (50°S–20°S) and matched the occurrence years of RPs.

Our study demonstrates that global warming caused $T_{air}^{max,gs}$ to exceed T_{opt}^{eco} at lower latitudes (45°N ~ 30°S) and the reversal of global greening to browning can be explained by the sustained global warming: growth would be reduced when $T_{air}^{max,gs}$ surpasses T_{opt}^{eco} at the RPs. Note that increased air temperature may stimulate the growth of PFTs with higher leaf-level optimum temperature (Huang et al., 2019), leading to expansion of those PFTs. Consequently, the grid level optimum temperature could also become higher. Significant PFT fraction changes were observed during the study period and ecosystem optimum temperature is defined on a coarse grid (0.05°) level, therefor, the PFT fraction change would bring uncertainty into our results.

Whereas in colder regions, that is, near the poles and at higher latitudes of the northern hemisphere (>50°N), $T_{air}^{max,gs}$ is still lower than T_{opt}^{eco}, suggesting that air temperature still exerts a positive influence on photosynthesis. To explain the existence of the reversal of greening-to-browning trends in these regions, we further analyzed contributions of the three key environmental variables (i.e., air temperature, VPD and root zone soil water content [RSW]) (see Section 2) to trend changes in growing season LAI during the period 1982–2018.

We further found that $T_{air}^{max,gs}$ significantly increased globally, VPD increased with weak changes at higher latitudes (>45°N), and RSW changed variably with obvious decreases at lower latitudes (10° N–30°S) (Figure

10.1029/2022EF002788

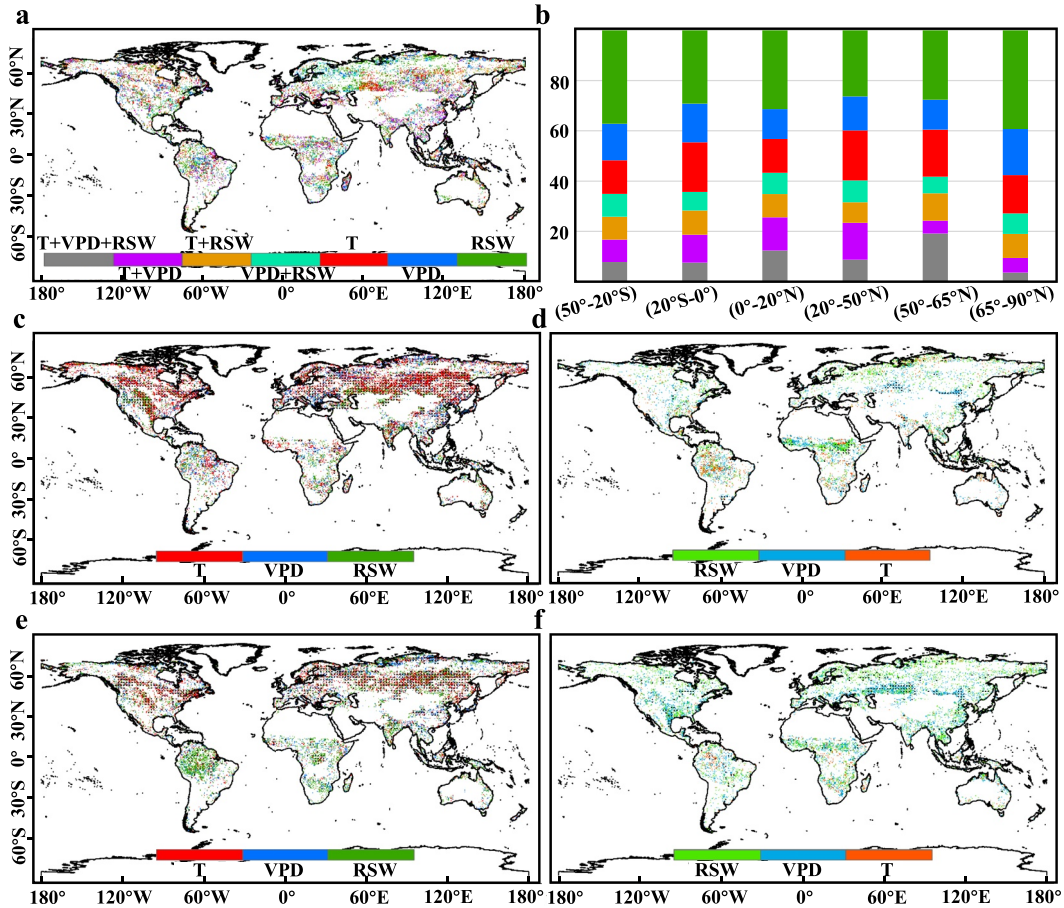

Figure 4. Comparison of the occurrence years of the reversal points (RPs) and trends of leaf area index (LAI) with that of environmental variables. The environmental variables include mean daily maximum air temperature in growing season ($T_{air}^{max,gs}$), vapor pressure deficit (VPD) and root zone water content (RSW). (a) Matching levels of the occurrence years of RPs. The selection criteria for matching level at each pixel is the occurrence years of RPs within 5 years, as $\left[RP_{LAI}^{year} - 5,\ RP_{LAI}^{year} + 5\right]$. Different color bars show matching levels for a single environmental variable or combination of variables, for example, the gray pixels with the label of (T + VPD + RSW) represent that the RPs of all the three variables matching LAI RPs. (b) The percentages of seven categories (classified in a) in six latitude regions. The best contributors (c, e positive; d, f negative) to LAI fitting trends before (c, d) and after (e), (f) RPs among the three environmental factors. The calculation methods for contributions of the three factors to LAI can be found in Section 2. The black dots in (c–f) indicate the Mann–Kendall test with $p < 0.1$.

S12–S14 in Supporting Information S1). LAI is sensitive to all the three environmental factors, on a global scale, and the sensitivity order of the three factors is $T_{air}^{max,gs}$ > RSW > VPD (before/after RPs: 0.483/0.469, 0.201/0.144, −0.270/−0.078 LAI m^2 m^{-2} $year^{-1}$, respectively, Figure S15 in Supporting Information S1). Air temperature maintains a positive effect on increasing LAI at high latitudes of the northern hemisphere because $T_{air}^{max,gs} < T_{opt}^{eco}$. LAI shows a negative correlation with VPD worldwide, with a stronger correlation in grass land in central Asia, northern Africa, and southern North America. Positive correlations between LAI and RSW were detected worldwide and negative correlations only in Saharan grassland region.

The trend fitting results show that the three environmental factors ($T_{air}^{max,gs}$, VPD and RSW) themselves also have significant RPs worldwide with global averaged occurrences of 1999, 2000, and 2000, respectively (Figures S12–S14 in Supporting Information S1). It is interesting that RP occurrence years of environmental factors match that of LAI well (Figure 4). The pixels with matched RPs between RSW and LAI account for 38% of the global vegetated land, the highest proportion among the three factors, mainly located at high latitudes of Eurasia (>45°N) (Figures 4a and 4b).

LAI in the arid areas of central and western Kazakhstan and southern Mongolia, and in southeastern China gradually decreased after the RPs, mainly caused by RSW decreasing and VPD increasing (Figures 4c–4d, Figures S15 and S16 in Supporting Information S1). Considering the decreasing trend of rainfall in southern China, the continuing increase of LAI may be due to human management and accompanied by continually increasing air temperature (Chen et al., 2019; Feng et al., 2021). The greening in southern India is mainly caused by the increase of rainfall and RSW; whereas LAI has continued to increase in northern India although both rainfall and RSW are decreasing, which may be attributed to agricultural management (Chen et al., 2019). A large-scale reduction in rainfall in North America around the occurrences of the LAI RPs, directly led to an increase in VPD and a decrease in RSW (Figures S17e–S17h in Supporting Information S1), offsetting enhancement of increasing temperature on LAI, as a result, the RP occurred, and vegetation is browning after RP (Figure 2a). In most parts of South America and Africa, VPD has gradually increased and RSW gradually decreased, leading to a decrease in LAI after the RPs (Figure 2a, Figures S17g–S17h in Supporting Information S1).

In summary, the reversal of vegetation greening to browning from this century at lower latitudes (45°N ~ 30°S) can be explained by increasing $T_{air}^{max,gs}$ exceeding T_{opt}^{eco} (Figure 3), while for most of rest of the world, it is caused by the combination of increasing VPD and decreasing RSW (Figure 4).

Conflict of Interest

The authors declare no conflicts of interest relevant to this study.

Data Availability Statement

There are three popular and state-of-arts LAI data sets used in this study, which are the AVHRR LAI data set, the GIMMS LAI3g LAI data set, and the GLASS LAI data set, and are respectively available at https://data.noaa.gov/dataset/dataset/noaa-climate-data-record-cdr-of-avhrr-leaf-area-index-lai-and-fraction-of-absorbed-photosynthet, http://sites.bu.edu/cliveg/datacodes/, and http://www.glass.umd.edu/Download.html. The climate data set (maximum and mean daily air temperature, vapor pressure deficit, actual vapor pressure) were acquired from the Climatic Research Unit (CRU), which are available at https://crudata.uea.ac.uk/cru/data/hrg/. The monthly RSW data were obtained from Modern-Era Retrospective analysis for Research and Applications Version 2 (MERRA-2) with a spatial resolution of 0.5° × 0.625° from 1982 to 2018, which are available at https://climatedataguide.ucar.edu/variables/land/soil-moisture. The land cover data set of GLASS-GLC product was obtained from the GLASS Climate Data Records (CDRs), which are available at https://doi.pangaea.de/10.1594/PANGAEA.913496. All the data and results developed in this study can be requested from corresponding author (baozhang.chen@igsnrr.ac.cn). The primary code is available at https://github.com/EFPaper2022EF002788code/LAIcode.git.

Acknowledgments
This research is founded by the National Key R&D Program of China (2018YFA0606001) and by the National Natural Science Foundation of China (41977404). We acknowledge constructive and insightful comments from Prof. Piao at Peking University.

References

Akaike, H. (1974). A new look at the statistical model identification. *IEEE Transactions on Automatic Control*, *19*, 716–723.

Akinwande, M. O., Dikko, H. G., & Samson, A. (2015). Variance inflation factor: As a condition for the inclusion of suppressor variable (s) in regression analysis. *Open Journal of Statistics*, *5*(07), 754–767. https://doi.org/10.4236/ojs.2015.57075

Baldocchi, D., Falge, E., Gu, L., Olson, R., Hollinger, D., Running, S., et al. (2001). FLUXNET: A new tool to study the temporal and spatial variability of ecosystem-scale carbon dioxide, water vapor, and energy flux densities. *Bulletin of the American Meteorological Society*, *82*(11), 2415–2434. https://doi.org/10.1175/1520-0477(2001)082<2415:fantts>2.3.co;2

Bonan, G. B., Pollard, D., & Thompson, S. L. (1992). Effects of boreal forest vegetation on global climate. *Nature*, *359*(6397), 716–718. https://doi.org/10.1038/359716a0

Chen, B., Xu, G., Coops, N. C., Ciais, P., Innes, J. L., Wang, G., et al. (2014). Changes in vegetation photosynthetic activity trends across the Asia–Pacific region over the last three decades. *Remote Sensing of Environment*, *144*, 28–41. https://doi.org/10.1016/j.rse.2013.12.018

Chen, C., Park, T., Wang, X., Piao, S., Xu, B., Chaturvedi, R. K., et al. (2019). China and India lead in greening of the world through land-use management. *Nature Sustainability*, *2*, 122–129. https://doi.org/10.1038/s41893-019-0220-7

Corlett, R. T. (2011). Impacts of warming on tropical lowland rainforests. *Trends in Ecology & Evolution*, *26*(11), 606–613. https://doi.org/10.1016/j.tree.2011.06.015

Cox, P. M., Betts, R. A., Jones, C. D., Spall, S. A., & Totterdell, I. J. (2000). Acceleration of global warming due to carbon-cycle feedbacks in a coupled climate model. *Nature*, *408*(6809), 184–187. https://doi.org/10.1038/35041539

de Jong, R., Verbesselt, J., Schaepman, M. E., & De Bruin, S. (2012). Trend changes in global greening and browning: Contribution of short-term trends to longer-term change. *Global Change Biology*, *18*(2), 642–655. https://doi.org/10.1111/j.1365-2486.2011.02578.x

Fang, H., Baret, F., Plummer, S., & Schaepman-Strub, G. (2019). An overview of global Leaf area Index (LAI): Methods, products, validation, and applications. *Reviews of Geophysics*, *57*(3), 739–799. https://doi.org/10.1029/2018rg000608

Feng, X., Fu, B., Zhang, Y., Pan, N., Zeng, Z., Tian, H., et al. (2021). Recent leveling off of vegetation greenness and primary production reveals the increasing soil water limitations on the greening Earth. *Science Bulletin*, *66*(14), 1462–1471. https://doi.org/10.1016/j.scib.2021.02.023

Field, C. B., Randerson, J. T., & Malmström, C. M. (1995). Global net primary production: Combining ecology and remote sensing. *Remote Sensing of Environment*, *51*(1), 74–88. https://doi.org/10.1016/0034-4257(94)00066-v

Forzieri, G., Alkama, R., Miralles, D. G., & Cescatti, A. (2017). Satellites reveal contrasting responses of regional climate to the widespread greening of Earth. *Science*, *356*(6343), 1180–1184. https://doi.org/10.1126/science.aal1727

Gelaro, R., McCarty, W., Suarez, M. J., Todling, R., Molod, A., Takacs, L., et al. (2017). The modern-era retrospective analysis for research and applications, version 2 (MERRA-2). *Journal of Climate*, *30*(14), 5419–5454. https://doi.org/10.1175/jcli-d-16-0758.1

Haberl, H., Erb, K. H., Krausmann, F., Gaube, V., Bondeau, A., Plutzar, C., et al. (2007). Quantifying and mapping the human appropriation of net primary production in earth's terrestrial ecosystems. *Proceedings of the National Academy of Sciences*, *104*(31), 12942–12947. https://doi.org/10.1073/pnas.0704243104

He, H., Wang, S., Zhang, L., Wang, J., Ren, X., Zhou, L., et al. (2019). Altered trends in carbon uptake in China's terrestrial ecosystems under the enhanced summer monsoon and warming hiatus. *National Science Review*, *6*(3), 505–514. https://doi.org/10.1093/nsr/nwz021

Huang, M., Piao, S., Ciais, P., Penuelas, J., Wang, X., Keenan, T. F., et al. (2019). Air temperature optima of vegetation productivity across global biomes. *Nat. Ecol. Evol.*, *3*(5), 772–779. https://doi.org/10.1038/s41559-019-0838-x

Jung, M., Reichstein, M., Schwalm, C. R., Huntingford, C., Sitch, S., Ahlstrom, A., et al. (2017). Compensatory water effects link yearly global land CO_2 sink changes to temperature. *Nature*, *541*(7638), 516–520. https://doi.org/10.1038/nature20780

Kattge, J., & Knorr, W. (2007). Temperature acclimation in a biochemical model of photosynthesis: A reanalysis of data from 36 species. *Plant, Cell and Environment*, *30*(9), 1176–1190. https://doi.org/10.1111/j.1365-3040.2007.01690.x

Law, B. E., Falge, E., Gu, L., Baldocchi, D., Bakwin, P., Berbigier, P., et al. (2002). Environmental controls over carbon dioxide and water vapor exchange of terrestrial vegetation. *Agricultural and Forest Meteorology*, *113*(1–4), 97–120. https://doi.org/10.1016/s0168-1923(02)00104-1

Liang, S., Zhao, X., Liu, S., Yuan, W., Cheng, X., Xiao, Z., et al. (2013). A long-term Global Land Surface Satellite (GLASS) data-set for environmental studies. *International Journal of Digital Earth*, *6*(sup1), 5–33. https://doi.org/10.1080/17538947.2013.805262

Liu, H., Gong, P., Wang, J., Clinton, N., Bai, Y., & Liang, S. (2020). Annual dynamics of global land cover and its long-term changes from 1982 to 2015. *Earth System Science Data*, *12*(2), 1217–1243. https://doi.org/10.5194/essd-12-1217-2020

Liu, Y. (2020). Optimum temperature for photosynthesis: From leaf-to ecosystem-scale. *Science Bulletin*, *65*(8), 601–604. https://doi.org/10.1016/j.scib.2020.01.006

Lloyd, J., & Farquhar, G. D. (2008). Effects of rising temperatures and [CO_2] on the physiology of tropical forest trees. *Philosophical Transactions of the Royal Society B: Biological Sciences*, *363*(1498), 1811–1817. https://doi.org/10.1098/rstb.2007.0032

Lucht, W., Prentice, I. C., Myneni, R. B., Sitch, S., Friedlingstein, P., Cramer, W., et al. (2002). Climatic control of the high-latitude vegetation greening trend and Pinatubo effect. *Science*, *296*(5573), 1687–1689. https://doi.org/10.1126/science.1071828

Piao, S., Wang, X., Ciais, P., Zhu, B., Wang, T., & Liu, J. (2011). Changes in satellite-derived vegetation growth trend in temperate and boreal Eurasia from 1982 to 2006. *Global Change Biology*, *17*(10), 3228–3239. https://doi.org/10.1111/j.1365-2486.2011.02419.x

Piao, S., Wang, X., Park, T., Chen, C., Lian, X., He, Y., et al. (2020). Characteristics, drivers and feedbacks of global greening. *Nature Reviews Earth & Environment*, *1*, 14–27. https://doi.org/10.1038/s43017-019-0001-x

Tian, F., Fensholt, R., Verbesselt, J., Grogan, K., Horion, S., & Wang, Y. (2015). Evaluating temporal consistency of long-term global NDVI datasets for trend analysis. *Remote Sensing of Environment*, *163*, 326–340. https://doi.org/10.1016/j.rse.2015.03.031

Tyree, M. T., & Dixon, M. A. (1986). Water stress induced cavitation and embolism in some woody plants. *Physiologia Plantarum*, *66*(3), 397–405. https://doi.org/10.1111/j.1399-3054.1986.tb05941.x

Wang, S., Zhang, Y., Ju, W., Chen, J. M., Ciais, P., Cescatti, A., et al. (2020). Recent global decline of CO_2 fertilization effects on vegetation photosynthesis. *Science*, *370*, 1295–1300. https://doi.org/10.1126/science.abb777

Williams, A. P., Allen, C. D., Macalady, A. K., Griffin, D., Woodhouse, C. A., Meko, D. M., et al. (2013). Temperature as a potent driver of regional forest drought stress and tree mortality. *Nature Climate Change*, *3*, 292–297. https://doi.org/10.1038/nclimate1693

Xu, G., Zhang, H., Chen, B., Zhang, H., Yan, J., Chen, J., et al. (2014). A bayesian based method to generate a synergetic land-cover map from existing land-cover products. *Remote Sensing*, *6*, 5589–5613. https://doi.org/10.3390/rs6065589

Xu, L., Myneni, R. B., Chapin, III, F. S., Callaghan, T. V., Pinzon, J. E., Tucker, C. J., et al. (2013). Temperature and vegetation seasonality diminishment over northern lands. *Nature Climate Change*, *3*(6), 581–586. https://doi.org/10.1038/nclimate1836

Yuan, W., Zheng, Y., Piao, S., Ciais, P., Lombardozzi, D., Wang, Y., et al. (2019). Increased atmospheric vapor pressure deficit reduces global vegetation growth. *Science Advances*, *5*(8), eaax1396. https://doi.org/10.1126/sciadv.aax1396

Zhu, Z., Piao, S., Myneni, R. B., Huang, M., Zeng, Z., Canadell, J. G., et al. (2016). Greening of the Earth and its drivers. *Nature Climate Change*, *6*(8), 791–795. https://doi.org/10.1038/nclimate3004